Intrinsic topology of various nodal rings in planar honeycomb lattices

Wei Xu [1], Yang Xue [2,*], Bao Zhao [3], Zhijian Li [1], and Zhongqin Yang [1,4,†]

[1]*State Key Laboratory of Surface Physics* and Department of Physics, *Fudan University*, Shanghai 200433, China
[2]*School of Science*, *East China University of Science and Technology*, Shanghai 200237, China
[3]*School of Physics Science and Information Technology, Shandong Key Laboratory of Optical Communication Science and Technology*, *Liaocheng University*, Liaocheng 252059, China
[4]*Shanghai Qi Zhi Institute*, Shanghai 200030, China

A universal topology is predicted for nodal-ring bands formed in planar honeycomb lattices through tight-binding models and topological quantum chemistry theories. In planar honeycomb lattices with s and p orbitals, various nodal-ring bands can occur due to the in-plane mirror symmetry. The band gaps of the nodal rings, opened by spin-orbit coupling, are all found being in quantum spin Hall insulating or topological crystalline insulating states. Two types of the intrinsic topologic states are observed in thallene with first-principles calculations, which has been fabricated in experiments. Our findings provide new routes to generate topologically nontrivial states in honeycomb lattices.

I. INTRODUCTION

Quantum spin Hall insulators (QSHIs) [1–4] and topological crystalline insulators (TCIs) [5–9] are two typical topological electronic states that have served as conceptual landmarks for the studies of topological materials. Both QSHIs and TCIs exhibit topology-protected edge states, bringing about quantized electronic transport. They are expected to have significant potential for low power information processing applications. The appearance of QSHIs and TCIs requires disparate symmetries. The former demands time-reversal symmetry while the latter calls for certain crystal symmetry protection [5]. The QSHIs have been experimentally validated in HgTe/CdTe [10] (also InAs/GaSb [11]) quantum wells and WTe$_2$ monolayers [12]. The TCIs have been observed not only in three-dimensional materials, such as SnTe [13] and Pb$_{1-x}$Sn$_x$Te [14], but also in two-dimensional (2D) SnTe monolayers [15], etc. Graphene, with a planar honeycomb lattice, is the first QSHI discovered theoretically [1,16,17]. Since the successful fabrication of graphene, the honeycomb lattice has become a seminal lattice and attracted widespread research interest. Other 2D group-IV film materials such as silicene [18], germanene [19], and stanene [20], all with a honeycomb lattice, were synthesized experimentally and found hosting quantum spin Hall effects. Besides, the group-V elements [21,22] can also form stable honeycomb structures. After hydrogen passivation, these honeycomb arsenic [23], stibium [4], and bismuth [24] all exhibit characteristics of QSHIs. Unique coherent many-body excitons were observed in NiPS$_3$ compounds with honeycomb lattices formed by Ni atoms [25]. The exotic quantum states, such as superconductivity [26], strong correlation effect [27],

and quantum anomalous Hall effect [28] recently observed in moiré graphene, have ulteriorly showcased the utmost significance of the honeycomb lattice.

Group-III honeycomb monolayers such as borophene and thallene were also reported in experiments. The borophene was grown on an Al (111) surface through molecular beam epitaxy method [29]. And the thallene was successfully fabricated on a single-layer NiSi$_2$ atop Si (111) substrate [30,31]. Unlike most monolayers composed of group-IV and group-V elements, the honeycomb lattices formed by the group-III elements (B and Tl) are completely flat rather than buckled [30–32]. This planar geometric structure, with an in-plane mirror symmetry (M_z), can lead to a high probability for the material possessing rare nodal-ring band structures [33,34], providing an excellent material platform for studying the unique electronic states of the nodal-ring bands. It has, however, not been intensively explored, to the best of our knowledge.

In this work, we study the topologic natures of the nodal rings formed in planar honeycomb lattices with s and p orbitals by using tight-binding (TB) models, topological quantum chemistry (TQC) theories, and density functional theory (DFT) calculations. Due to the flat lattice, diverse nodal rings at different momenta are achieved. The band gaps of the nodal rings, opened by spin-orbit coupling (SOC), are all found being in topologically nontrivial TCI or QSHI states. The predicted topological behaviors are observed in thallene and indiumene (the indium monolayer). Our results provide an understanding for the topology of the nodal lines in honeycomb lattices, promoting the potential applications of the lattices in topological nanoelectronics.

II. COMPUTATIONAL METHODS

Our first-principles DFT calculations are carried out with the generalized gradient approximation proposed by Perdew,

*Contact author: xuey@ecust.edu.cn
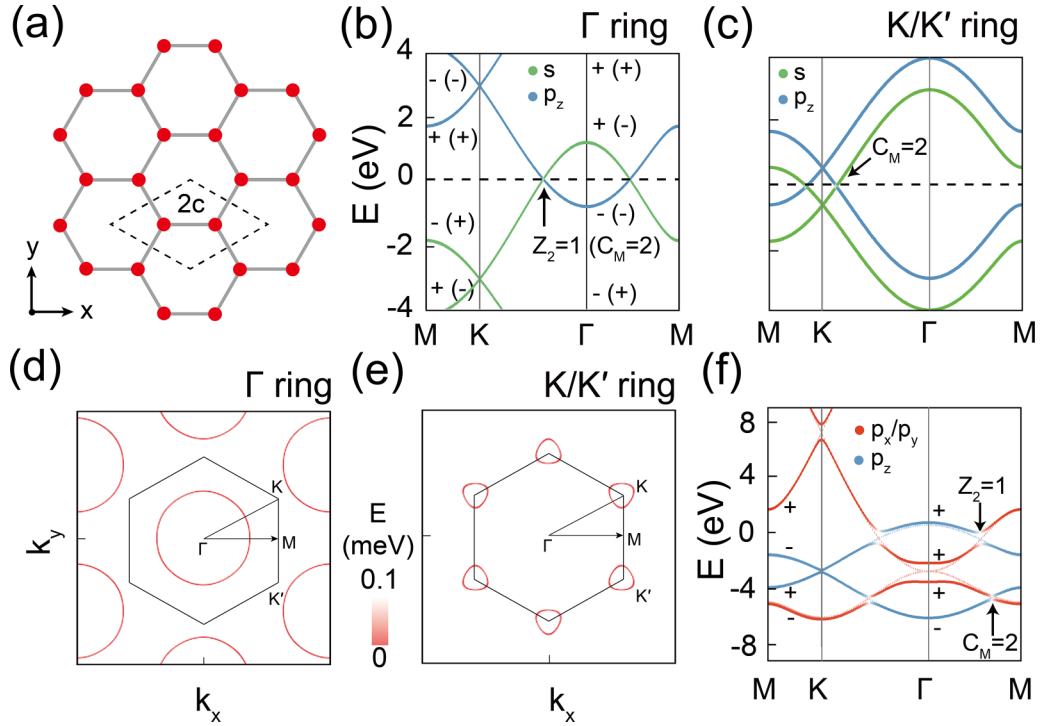†Contact author: zyang@fudan.edu.cn

FIG. 1. (a) The planar honeycomb lattice. The two red sites in the unit cell (dashed rhombus) are both at $2c$ Wyckoff positions. (b) The Γ ring composed of the $s-p_z$ orbitals at energy zero, obtained with the TB parameters (in eV): $E_s = -3$, $E_x = 100$, $E_y = 100$, $E_z = 3$, $V_{ss\sigma} = -1.3$, $V_{sp\sigma} = 1.81$, $V_{pp\pi} = -1.13$, $V_{pp\sigma} = 2.11$, and $\lambda = 1$. The parities of the energy levels near the energy zero at the TRIPs are listed. The parities in parentheses are obtained by only changing the sign of $V_{ss\sigma}$ ($V_{ss\sigma} = 1.3$ eV). (c) The K/K' ring composed of the $s-p_z$ orbitals at energy zero, obtained with the TB parameters of $E_s = -0.5$ eV and $E_z = 0.5$ eV. The other TB parameters are the same as those defined in (b). (d), (e) The difference between the energies of the two crossing bands in the Γ rings of (b) and K/K' rings of (c) in the 2D BZ, respectively, but with $\lambda = 0$. The middle hexagon depicts the first BZ. (f) Two Γ rings composed of p_x/p_y-p_z orbitals at energy zero and -5 eV, obtained with the TB parameters (in eV): $E_s = 100$, $E_x = 8$, $E_y = 8$, $E_z = -3$, $V_{ss\sigma} = 0$, $V_{sp\sigma} = 0$, $V_{pp\pi} = -1.13$, $V_{pp\sigma} = 8$, $\lambda = 0.6$. The parities at the TRIPs are also shown. Dashed curves give the bands without SOC ($\lambda = 0.0$).

Burke, and Ernzerhof (PBE) [35], which is implemented in the Vienna *ab initio* simulation package (VASP) [36]. The plane-wave cutoff energy is set to 500 eV and the vacuum space is taken to be more than 15 Å to avoid the influence between two adjacent slabs. The convergence criterions for the forces and total energies are 0.01 eV/Å and 10^{-6} eV, respectively. The $12 \times 12 \times 1$ Γ−centered k-point grids are employed to perform the integral in the first Brillouin zone. The topological properties, including evolution of the Wannier charge center (WCC), $\mathbb{Z}_2$, and edge states are investigated by constructing the maximal localized Wannier functions [37] using the WANNIER90 package [38] combined with the WANNIERTOOLS code [39]. To verify the correctness of the PBE calculations, hybrid-functional methods based on the Heyd-Scuseria-Ernzerhof (HSE)06 [40] scheme is adopted for the electronic structures of thallene.

III. RESULTS AND DISCUSSION

The band structures of a 2D planar honeycomb lattice, obtained from a TB model, are first introduced. As illustrated in Fig. 1(a), there are two sites per unit cell. At each site, four types of orbitals of $|s_{\uparrow\downarrow}\rangle$, $|p_{x\uparrow\downarrow}\rangle$, $|p_{y\uparrow\downarrow}\rangle$, and $|p_{z\uparrow\downarrow}\rangle$ are considered, where the up and down arrows indicate the spin indices. The Hamiltonian of the lattice could be written

as

$$H = H_0 + H_{\text{soc}}, \quad (1)$$

where the two terms in H are given by

$$H_0 = \sum_{\alpha,i,\sigma} c^{\dagger}_{\alpha i\sigma} E_i c_{\alpha i\sigma} + \sum_{\alpha,\beta,i,j,\sigma} c^{\dagger}_{\alpha i\sigma} t_{\alpha\beta ij} c_{\beta j\sigma}, \quad (2)$$

$$H_{\text{soc}} = \lambda \vec{L} \cdot \vec{S}. \quad (3)$$

In Eq. (2), $c^{\dagger}_{\alpha i\sigma}$ ($c_{\alpha i\sigma}$) represents a creation (annihilation) operator for an electron with spin σ and orbital i on site α. E_i is the on-site energy for orbital i. $t_{\alpha\beta ij}$ is the nearest-neighbor hopping integral which can be expressed through the Slater-Koster (SK) integrals [41]. In Eq. (3), H_{soc} represents the on-site SOC term. The λ parameter is the atomic SOC strength. The detailed derivations of H_0 and H_{soc} based on the SK integrals are provided in part I (A) of the Supplemental Material (SM) [42].

The coupling between different orbitals can lead to the emergence of diverse nodal-ring band structures. We now discuss the nodal rings composed of s and p_z orbitals [Figs. 1(b) and 1(c)]. In this case, two types of nodal rings centered at Γ and K/K' points can occur, called Γ rings [Fig. 1(b)] and K/K' rings [Fig. 1(c)], respectively. The difference between the energies of the two crossing bands for the Γ rings and

TABLE I. The various topological nodal rings formed by different combinations of s and p orbitals. The possible topological states obtained for each case are given. The QSHI and TCI states will exchange to each other by varying the band parities, except for the states (marked in italic) of the K/K′ rings with $s-p_x/p_y$ orbitals.

Orbital combination	Band structure	Topological states
$s-p_x/p_y$	Γ ring	QSHI, TCI
	K/K′ ring	*QSHI, TCI*
$s-p_z$	Γ ring	QSHI, TCI
	K/K′ ring	TCI
p_x/p_y-p_z	Γ ring	QSHI, TCI
	K/K′ ring	TCI

K/K′ rings (both without SOC) in the 2D Brillouin zone (BZ) are displayed in Figs. 1(d) and 1(e), respectively. Regular rings and rings with a C_3 symmetry are clearly seen for the Γ ring [Fig. 1(d)] and K/K′ ring [Fig. 1(e)], respectively. The different shapes of the two types of rings are associated with the little-group symmetries at the Γ and K/K′ points. Due to the combination of the three symmetries in the planar honeycomb lattice: M_z, space inversion symmetry (P), and time-reversal symmetry ($\mathcal{T}$), band gaps can be opened for all the nodal rings when the SOC is considered (the derivation is given in SM part I (B) [42]). In Figs. 1(b) and 1(c), small band gaps of 3 meV are opened at energy zeros, which can be ascribed to zero SOC between s and p_z orbitals and small SOC interactions from the p_x/p_y and p_z orbitals through the hybridization effect. Note that despite the gaps opened, we still call them Γ rings or K/K′ rings due to remaining of the loop band characteristic.

Since the honeycomb lattice has the P symmetry, we can calculate the topological invariant $\mathbb{Z}_2$ from parities of the energy levels at the time-reversal invariant points (TRIPs) in the BZ [43] to analyze the topological behavior of the nodal rings under SOC. For the Γ ring displayed in Fig. 1(b), the parities of the occupied states at the TRIPs yield $\mathbb{Z}_2 = 1$. The evolution of the WCC is also calculated [Fig. S1(a)], which as well as the $\mathbb{Z}_2 = 1$ indicates a QSHI achieved for the Γ ring. To dig other possible topological states in this case, we change the sign of $V_{ss\sigma}$ (from -1.3 eV to 1.3 eV), reflecting the hopping interactions of the s orbitals from the neighbor atoms. We find that the band structures do not change while the parities of the energy levels coming from the s orbital all become opposite, given in the brackets in Fig. 1(b). These parities result in $\mathbb{Z}_2 = 0$. Hence, the quantum spin Hall state disappears in the lattice.

In the honeycomb lattice, the entire 2D BZ is invariant under M_z symmetry. For spinful system (with SOC), the M_z symmetry has the eigenvalues of $+i$ and $-i$. Thus, the states of the lattice can be categorized into mirror-even and mirror-odd subspaces. Consequently, the M_z-eigenvalue-resolved WCC spectra can be calculated. As illustrated in Fig. S1(b), the intersections between the WCC spectra with the different mirror parities are robust and protected by the M_z symmetry [5]. Moreover, the WCC spectrum associated with the $+i$ eigenvalue in Fig. S1(b) exhibits a winding number $C_+ = 2$, whereas that associated with the $-i$ eigenvalue has a winding

number $C_- = -2$. Therefore, a mirror Chern number $C_M = (C_+ - C_-)/2 = 2$ is obtained, leading to a TCI acquired for this situation [Fig. 1(b)] with $V_{ss\sigma} = 1.3$ eV. The topological behavior of the band gap for the K/K′ ring [Fig. 1(c)] can be analyzed similarly. The calculated topological invariant $\mathbb{Z}_2 = 0$ for the small band gap (opened by the SOC) in the K/K′ ring. This $\mathbb{Z}_2$ value does not change even if the sign of $V_{ss\sigma}$ becomes opposite owing to the even occupied energy levels at the TRIPs. The M_z-eigenvalue-resolved WCC spectra [Fig. S1(c)] gives that the K/K′ ring is in a TCI phase with $C_M = 2$. Different from the case of the Γ ring, no QSHI phase can be achieved in the K/K′ ring. The topological states acquired in the nodal rings composed of $s-p_z$ orbitals are summarized in Table I.

Figure 1(f) demonstrates the TB bands with two Γ rings composed of p_x/p_y-p_z orbitals, which are located at energy zero and -5 eV. The calculated corresponding WCC spectra are displayed in Figs. S2(a) and 2(b), respectively. Explicitly, the SOC-induced band gap for the Γ ring at energy zero is in a QSHI phase while the one for the Γ ring at -5 eV is in a TCI phase. If we increase E_z from -10 eV [Fig. 1(f)] to -2 eV, K/K′ rings occur at 4.3 eV [Fig. S2(c)]. Similar to the cases for the K/K′ rings with $s-p_z$ orbitals [Fig. 1(c)], the band gap for the K/K′ rings in Fig. S2(c) falls within a TCI phase [Fig. S2(d)]. The analysis of the cases for the nodal rings with $s-p_x/p_y$ orbitals is similar. These TB results are also listed in Table I, showing that the SOC-induced band gaps in the nodal rings composed of s and p orbitals are all topologically nontrivial.

The general topological nature of the nodal rings composed of s and p orbitals in the lattice can be disclosed by using TQC theories. The planar honeycomb lattice has a space group of No.191. The two sites in the unit cell are located at $2c$ maximal Wyckoff positions [Fig. 1(a)]. The site-symmetry group of the position is D_{3h} ($\bar{6}m2$), which has six different irreducible representations (irreps) A_1', A_2', E', A_1'', A_2'', and E'' (Table S1). When s or p orbitals are placed at one of the $2c$ sites, they must be arranged according to the basis of the irreps of D_{3h}. Thus, the s and p orbitals on the $2c$ site can be divided into three groups (s, p_x/p_y, p_z). Each group belongs to the different irreps of D_{3h}, inducing three distinct elementary band representations (EBRs) [44,45]. To understand the topological behaviors of the Γ and K rings, Table S2 presents the irreps of the little groups at these two high-symmetry points for various EBRs. For a nodal ring, generally formed by two crossing bands, SOC induces a splitting of the degenerate points. If the occupied part in the two segments of the energy bands (separated by the SOC) cannot individually form an EBR, the band gap in the nodal ring is topologically nontrivial [44,45].

Due to the $2c$ site being the maximal Wyckoff position, the s and p orbitals on this site will induce the EBRs that cannot be further separated into new EBRs [44–47]. As shown in Table S2, different groups of the orbitals (s, p_x/p_y, or p_z) have distinct EBRs. Consequently, a nodal ring comprising only single component (s, p_x/p_y, or p_z) cannot be split into new EBRs. The band gap opened by SOC in these single-component nodal rings must be in a topologically nontrivial state. For nodal rings composed of $s-p_z$ or p_x/p_y-p_z bands, since there are no interactions between $s-p_z$ (and also p_x/p_y-p_z), the EBRs of p_z bands are independent of those of s (or
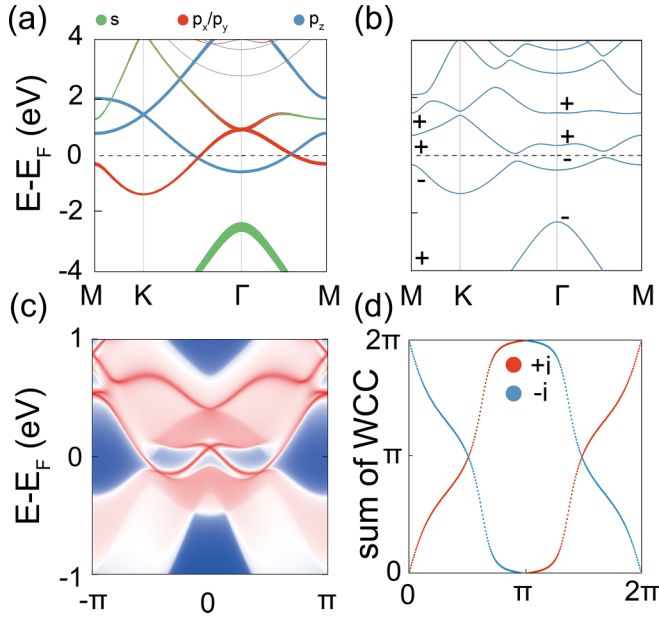
FIG. 2. The DFT results for thallene. (a) The orbital-resolved band structure without SOC. (b) The band structure with SOC. (c) Edge states of thallene along the [100] direction. (d) Evolution of the WCCs along the k_y.

p_x/p_y) bands. Therefore, a nodal ring consisting of $s-p_z$ or p_x/p_y-p_z bands will encompass two different EBRs. These EBRs will undergo splitting into non-EBRs when SOC opens a band gap for the nodal ring. These topologically nontrivial cases can be actually confirmed by the results in Figs. 1(b), 1(c), 1(f), and S2(c), discussed above through the TB model.

For nodal rings composed of s and p_x/p_y, the situation becomes somewhat complex due to the hopping between s and p_x/p_y orbitals in the lattice. As shown in Table S3, three different EBR decompositions, induced from the Wyckoff positions of $1a$, $2c$, and $3f$, are obtained. Due to the absence of identical 1D irreps at the Γ point (or K/K' point) for any different EBRs contained within a decomposition, the SOC-induced band gap leads to the emergence of non-EBRs. Hence, in a planar honeycomb lattice with s and p orbitals, the band gaps opened by SOC in the nodal-ring bands at Γ or K/K' points are all topologically nontrivial.

Topological properties of thallene and indiumene. Thallene, already synthesized in experiments [30,31], owns a planar honeycomb lattice. Based on the DFT and TB model calculations, we find thallene is a TCI with $C_M = 2$, instead of an ordinary insulator [48]. The fully optimized lattice parameters for thallene are $a = b = 5.26$ Å [Fig. S3(a)]. The bands around the Fermi level (E_F) of thallene [Fig. 2(a)] are predominantly contributed by the p orbitals. The p_z bands form a doubly degenerate point, namely the Dirac point, at the K point (about 1.7 eV), akin to the Dirac point found in the 2D seminal material of graphene [49]. Interestingly, the p_x/p_y bands are degenerate at the Γ point with the energy close to that of the Dirac point at the K point. This band characteristic of two doubly degenerate points in thallene without SOC is very similar to that of the plumbene [50]. The two doubly degenerate points in plumbene both occur at the E_F due to

one more valence electron in a Pb atom than in a Tl atom. The p_x/p_y bands intersect with the p_z (also some s) bands near the K/K' and Γ points, resulting in two nodal rings: the Γ ring (~0 eV) and the K/K' ring (~2.5 eV). Upon inclusion of SOC, not only does the degeneracy at high-symmetry points split, but also the accidental degeneracy of nodal rings lifts. The latter trend is accordant to the conclusion made above from the symmetry analysis. Thus, a global band gap (about 144 meV) is opened around E_F in the material, as depicted in Fig. 2(b). Since the PBE functional often underestimates band gaps, we check the bands by using the HSE06 functional which yields an enlarged energy gap of about 212 meV [Figs. S3(b) and S3(c)]. The band dispersion of HSE06 is very similar to that of PBE.

Our analysis has demonstrated that the SOC-induced band gap in a Γ ring composed of p_x/p_y-p_z band must be a QSHI or a TCI [Fig. 1(f) and Table I]. Hence, thallene shall be a QSHI with $\mathbb{Z}_2 = 1$ or a TCI with $C_M = 2$. The parity calculations [Fig. 2(b)] give $\mathbb{Z}_2 = 0$ for thallene, inferring the monolayer being a TCI. To illustrate its topological properties, we calculate edge states of the semi-infinite thallene. Two pairs of edge states emerge within the bulk gap [Fig. 2(c)], signifying the nontrivially topologic nature of the global band gap in thallene. The edge states are also confirmed in a thallene nanoribbon [Fig. S3(d)]. The WCC spectra with the eigenvalues of $+i$ and $-i$ intersect in Fig. 2(d), also proving thallene being a TCI with $C_M = 2$. This result is different from the conclusion of an ordinary insulator in Ref. [48], made based on $\mathbb{Z}_2 = 0$.
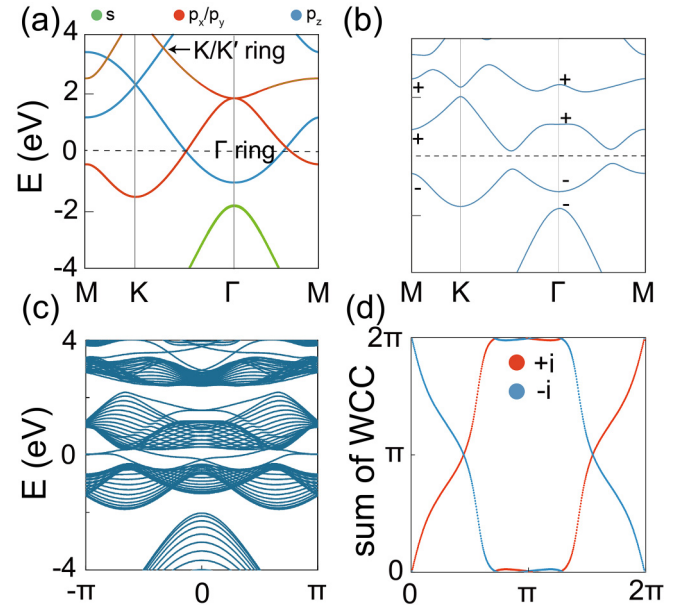

FIG. 3. The TB results for thallene. (a) The band structure with the TB parameters (in eV): $E_s = -7$, $E_x = 3$, $E_y = 3$, $E_z = 2$, $V_{ss\sigma} = -1.3$, $V_{sp\sigma} = 1.82$, $V_{pp\pi} = -1.13$, $V_{pp\sigma} = 2.11$, and $\lambda = 0$. A Γ ring and a K/K' ring are discovered at E_F and 3.3 eV, respectively. (b) The band structure with SOC ($\lambda = 0.6$ eV). The other parameters are the same as in (a). The parities at Γ and M points are also shown. (c) The band structure for a thallene nanoribbon. (d) The M_z-eigenvalue-resolved WCCs along the k_y for the band gap of the Γ ring.
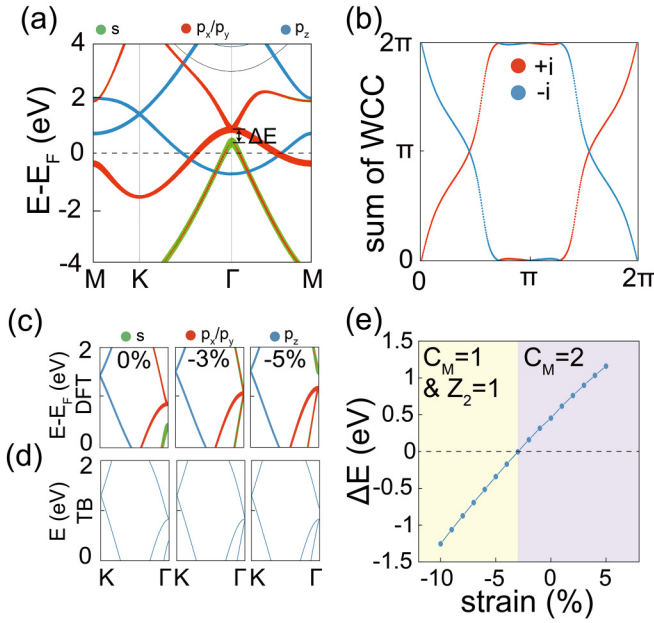
FIG. 4. (a) The orbital-resolved DFT band structure of indiumene without SOC. (b) Evolution of the WCCs for the indiumene without strain. (c) The DFT band structures of indiumene with various compressive strain strengths. From left to right, the compressive strain strengths are 0%, 3%, and 5%, respectively. (d) The TB bands. From left to right, the $V_{ss\sigma}$ values are -1.45, -1.57, and -1.65 eV, respectively. (e) The ΔE as function of strain, where ΔE is defined in Fig. 4(a). The negative value of ΔE indicates band-inversion appearance.

We now comprehend the band structure of thallene from the TB model. The obtained TB results [Figs. 3(a) and 3(b)] for thallene can describe well the band characteristic given by the DFT calculations [Figs. 2(a) and 2(b)]. As depicted in Fig. 3(c), the Γ ring at the E_F and the K/K' ring at 3.3 eV both possess two pairs of topology-protected edge states. The M_z-eigenvalue-resolved WCCs for the Γ ring from the TB model [Fig. 3(d)] is also in good agreement with that from DFT calculations [Fig. 2(d)]. Both the WCC evolutions for the K/K' rings obtained from DFT [Fig. 2(a)] and TB model [Fig. 3(a)] for thallene are also calculated and given in Figs. S4(a) and S4(b), which imply a TCI phase obtained for the SOC-induced band gaps in the K/K' rings. This tendency is in line with the conclusion in the last row in Table I. Flat group-V (Sb or Bi) monolayers haven been reported to being TCIs with $C_M = 2$ [51], which actually belong to the last case in Table I.

The indium monolayer, called indiumene, with a flat honeycomb lattice exhibits a similar band structure [Fig. 4(a)] to that of thallene [Fig. 2(a)]. However, owing to its smaller atomic number and the shorter In-In bond lengths [Fig. S3(a)], not only is the energy level of the s orbital elevated [52], but the $V_{ss\sigma}$ strength becomes larger. The latter factor also leads to the s-orbital band around the Γ point moving up in energy

and crossing the E_F. Thus, the indiumene is a metal even if the SOC is considered (Fig. S5(a)). Although the s band intersects with the p_z band around the Γ point, it does not break the Γ ring composed of $p_x/p_y - p_z$ orbitals. Hence, the band gap around the E_F still possesses a C_M of 2, as depicted in Fig. 4(b).

Strain is an effective approach for tuning electronic and topological properties of real materials. For indiumene, strain can significantly affect the bands around the E_F. As demonstrated in Fig. 4(c), the s band in indiumene moves up in energy as the increase of the compressive strain strength. The s and p_x/p_y bands flip at -3% strain, accompanied by the ΔE [defined in Fig. 4(a)] becoming negative. The going up of the s band in Fig. 4(c) can be rationalized well by the increase of the absolute value of the $V_{ss\sigma}$ [Fig. 4(d)] due to the shorter In-In bond in the process. Thus, a topological phase transition happens in the indiumene with -3% strain. The phase diagram as a function of the strain is given in Fig. 4(e). Since the s band disrupts the original structure of the p_x/p_y bands in the monolayer with a compressive strain strength larger than 3%, the C_M becomes 1 in these cases, as indicated in Fig. S5(c) which also gives $\mathbb{Z}_2 = 1$. To confirm the results of $\mathbb{Z}_2 = 1$, we break the M_z symmetry of the monolayer with $\Delta E < 0$ (under such as -5% strain) by moving one atom in the unit cell along the z direction. The WCC evolution in Fig. S5(d) also clearly gives $\mathbb{Z}_2 = 1$. Hence, an interesting composite topological state of a TCI ($C_M = 1$) and a QSHI ($\mathbb{Z}_2 = 1$) is achieved for the indiumene with a compressive strain strength larger than 3%.

IV. CONCLUSIONS

From TB models and topological quantum chemistry theories, we find an intrinsic topological behavior for the nodal rings formed in flat honeycomb lattices with s and p orbitals. The SOC-induced band gaps in the nodal rings centered at Γ or K/K' points are all topologically nontrivial, being in QSHI or TCI phases. Our density functional theory calculations show that thallene is a TCI with $C_M = 2$, rather than an ordinary insulator, in line with the predictions achieved from the TQC theories. We also find that the indiumene can possess an exotic composite topologic state of a TCI ($C_M = 1$) and QSHI ($\mathbb{Z}_2 = 1$). The forming mechanism is analyzed. Our findings provide an understanding of the topological nature for the nodal-ring structure in the mature 2D honeycomb lattice materials, reinforcing the theoretical foundations for promising applications.

[1] C. L. Kane and E. J. Mele, Z_2 topological order and the quantum spin Hall effect, Phys. Rev. Lett. **95**, 146802 (2005).

[2] B. Fu, Y. Ge, W. Su, W. Guo, and C.-C. Liu, A new kind of 2D topological insulators BiCN with a giant gap and its substrate effects, Sci. Rep. **6**, 30003 (2016).

[3] D. N. Sheng, Z. Y. Weng, L. Sheng, and F. D. M. Haldane, Quantum spin-hall effect and topologically invariant Chern numbers, Phys. Rev. Lett. **97**, 036808 (2006).

[4] Z. Song, C.-C. Liu, J. Yang, J. Han, M. Ye, B. Fu, Y. Yang, Q. Niu, J. Lu, and Y. Yao, Quantum spin Hall insulators and quantum valley Hall insulators of BiX/SbX (X = H, F, Cl and Br) monolayers with a record bulk band gap, NPG Asia Mater **6**, e147 (2014).

[5] L. Fu, Topological crystalline insulators, Phys. Rev. Lett. **106**, 106802 (2011).

[6] T. H. Hsieh, H. Lin, J. Liu, W. Duan, A. Bansil, and L. Fu, Topological crystalline insulators in the SnTe material class, Nat. Commun. **3**, 982 (2012).

[7] Y. Ando and L. Fu, Topological crystalline insulators and topological superconductors: from concepts to materials, Annu. Rev. Condens. Matter Phys. **6**, 361 (2015).

[8] Y. Qian, Z. Tan, T. Zhang, J. Gao, Z. Wang, Z. Fang, C. Fang, and H. Weng, Layer construction of topological crystalline insulator LaSbTe, Sci. China Phys. Mech. Astron. **63**, 107011 (2020).

[9] R. Kim, B.-J. Yang, and C. H. Kim, Crystalline topological dirac semimetal phase in rutile structure $\beta' - PtO_2$, Phys. Rev. B **99**, 045130 (2019).

[10] B. A. Bernevig, T. L. Hughes, and S.-C. Zhang, Quantum spin Hall effect and topological phase transition in HgTe quantum wells, Science **314**, 1757 (2006).

[11] C. Liu, T. L. Hughes, X.-L. Qi, K. Wang, and S.-C. Zhang, Quantum spin Hall effect in inverted type-II semiconductors, Phys. Rev. Lett. **100**, 236601 (2008).

[12] S. Tang, C. Zhang, D. Wong, Z. Pedramrazi, H. Tsai, C. Jia, B. Moritz, M. Claassen, H. Ryu, S. Kahn *et al.*, Quantum spin Hall state in monolayer 1T′ − WTe$_2$, Nat. Phys. **13**, 683 (2017).

[13] Y. Tanaka, Z. Ren, T. Sato, K. Nakayama, S. Souma, T. Takahashi, K. Segawa, and Y. Ando, Experimental realization of a topological crystalline insulator in SnTe, Nat. Phys **8**, 800 (2012).

[14] S. Y. Xu, C. Liu, N. Alidoust, M. Neupane, D. Qian, I. Belopolski, J. D. Denlinger, Y. J. Wang, H. Lin, L. A. Wray *et al.*, Observation of a topological crystalline insulator phase and topological phase transition in Pb$_{1−x}$Sn$_x$Te, Nat. Commun. **3**, 1192 (2012).

[15] J. Liu, T. H. Hsieh, P. Wei, W. Duan, J. Moodera, and L. Fu, Spin-filtered edge states with an electrically tunable gap in a two-dimensional topological crystalline insulator, Nat. Mater. **13**, 178 (2014).

[16] C. L. Kane and E. J. Mele, Quantum spin Hall effect in graphene, Phys. Rev. Lett. **95**, 226801 (2005).

[17] M. Gmitra, S. Konschuh, C. Ertler, C. Ambrosch-Draxl, and J. Fabian, Band-Structure topologies of graphene: spin-orbit coupling effects from first principles, Phys. Rev. B **80**, 235431 (2009).

[18] A. Fleurence, R. Friedlein, T. Ozaki, H. Kawai, Y. Wang, and Y. Yamada-Takamura, Experimental evidence for epitaxial silicene on diboride thin films, Phys. Rev. Lett. **108**, 245501 (2012).

[19] M. Derivaz, D. Dentel, R. Stephan, M.-C. Hanf, A. Mehdaoui, P. Sonnet, and C. Pirri, Continuous germanene layer on Al(111), Nano Lett. **15**, 2510 (2015).

[20] Y. Xu, P. Tang, and S.-C. Zhang, Large-Gap quantum spin Hall states in decorated stanene grown on a substrate, Phys. Rev. B **92**, 081112(R) (2015).

[21] S. Zhang, M. Xie, F. Li, Z. Yan, Y. Li, E. Kan, W. Liu, Z. Chen, and H. Zeng, Semiconducting group 15 monolayers: A broad range of band gaps and high carrier mobilities, Angew. Chem. **128**, 1698 (2016).

[22] F. Reis, G. Li, L. Dudy, M. Bauernfeind, S. Glass, W. Hanke, R. Thomale, J. Schäfer, and R. Claessen, Bismuthene on a SiC substrate: A candidate for a high-temperature quantum spin Hall material, Science **357**, 287 (2017).

[23] J. Zhao, Y. Li, and J. Ma, Quantum spin Hall insulators in functionalized arsenene (AsX, X = F, OH and CH$_3$) monolayers with pronounced light absorption, Nanoscale **8**, 9657 (2016).

[24] H. Fahrvandi, E. Nadimi, and M. Schreiber, First-principles investigation of two-dimensional topological insulators BiX (X = H, F, O), Semicond. Sci. Technol. **35**, 085033 (2020).

[25] S. Kang, K. Kim, B. H. Kim, J. Kim, K. L. Sim, J. U. Lee, S. Lee, K. Park, S. Yun, T. Kim *et al.*, Coherent many-body exciton in van der Waals antiferromagnet NiPS$_3$, Nature (London) **583**, 785 (2020).

[26] Y. Cao, J. M. Park, K. Watanabe, T. Taniguchi, and P. Jarillo-Herrero, Pauli-limit violation and re-entrant superconductivity in moiré graphene, Nature (London) **595**, 526 (2021).

[27] G. Chen, A. L. Sharpe, E. J. Fox, Y. Zhang, S. Wang, L. Jiang, B. Lyu, H. Li, K. Watanabe, T. Taniguchi *et al.*, Tunable correlated Chern insulator and ferromagnetism in a moiré superlattice, Nature (London) **579**, 56 (2020).

[28] M. Serlin, C. L. Tschirhart, H. Polshyn, Y. Zhang, J. Zhu, K. Watanabe, T. Taniguchi, L. Balents, and A. F. Young, Intrinsic quantized anomalous Hall effect in a moiré heterostructure, Science **367**, 900 (2020).

[29] W. Li, L. Kong, C. Chen, J. Gou, S. Sheng, W. Zhang, H. Li, L. Chen, P. Cheng, and K. Wu, Experimental realization of honeycomb borophene, Sci. Bull. **63**, 282 (2018).

[30] D. V. Gruznev, L. V. Bondarenko, A. Y. Tupchaya, A. N. Mihalyuk, S. V. Eremeev, A. V. Zotov, and A. A. Saranin, Thallene: Graphene-like honeycomb lattice of Tl atoms frozen on single-layer NiSi$_2$, 2D Mater. **7**, 045026 (2020).

[31] A. N. Mihalyuk, L. V. Bondarenko, A. Y. Tupchaya, Y. E. Vekovshinin, T. V. Utas, D. V. Gruznev, J.-P. Chou, S. V. Eremeev, A. V. Zotov, and A. A. Saranin, Large-scale thallene film with emergent spin-polarized states mediated by tin intercalation for spintronics applications, Mater. Today Adv. **18**, 100372 (2023).

[32] Q. Zhong, L. Kong, J. Gou, W. Li, S. Sheng, S. Yang, P. Cheng, H. Li, K. Wu, and L. Chen, Synthesis of borophene nanoribbons on Ag(110) surface, Phys. Rev. Mater. **1**, 021001(R) (2017).

[33] R.-W. Zhang, C.-C. Liu, D.-S. Ma, and Y. Yao, From node-line semimetals to large-gap quantum spin Hall states in a family of pentagonal Group-IVA chalcogenide, Phys. Rev. B **97**, 125312 (2018).

[34] H. Bao, H. Zhao, Y. Xue, H. Huan, G. Gao, X. Liu, and Z. Yang, Various half-metallic nodal loops in organic Cr$_2$N$_6$C$_3$ monolayers, Nanoscale **13**, 3161 (2021).

[35] J. P. Perdew, K. Burke, and M. Ernzerhof, Generalized gradient approximation made simple, Phys. Rev. Lett. **77**, 3865 (1996).

[36] G. Kresse and J. Furthmüller, Efficient iterative schemes for *ab initio* total-energy calculations using a plane-wave basis set, Phys. Rev. B **54**, 11169 (1996).

[37] G. H. Wannier, The structure of electronic excitation levels in insulating crystals, Phys. Rev. **52**, 191 (1937).

[38] A. A. Mostofi, J. R. Yates, Y.-S. Lee, I. Souza, D. Vanderbilt, and N. Marzari, WANNIER90: A tool for obtaining maximally localised wannier functions, Comput. Phys. Commun. **178**, 685 (2008).

[39] Q. Wu, S. Zhang, H.-F. Song, M. Troyer, and A. A. Soluyanov, WANNIERTOOLS: An open-source software package for novel topological materials, Comput. Phys. Commun. **224**, 405 (2018).

[40] J. Heyd, G. E. Scuseria, and M. Ernzerhof, Hybrid functionals based on a screened coulomb potential, J. Chem. Phys. **118**, 8207 (2003).

[41] J. C. Slater and G. F. Koster, Simplified LCAO method for the periodic potential problem, Phys. Rev. **94**, 1498 (1954).

[42] See Supplemental Material at http://link.aps.org/supplemental/10.1103/PhysRevB.110.035418 for theory-related deduction and more results, which also includes Refs. [34,53].

[43] L. Fu and C. L. Kane, Topological insulators with inversion symmetry, Phys. Rev. B **76**, 045302 (2007).

[44] B. Bradlyn, L. Elcoro, M. G. Vergniory, J. Cano, Z. Wang, C. Felser, M. I. Aroyo, and B. A. Bernevig, Band connectivity for topological quantum chemistry: Band structures as a graph theory problem, Phys. Rev. B **97**, 035138 (2018).

[45] B. Bradlyn, L. Elcoro, J. Cano, M. G. Vergniory, Z. Wang, C. Felser, M. I. Aroyo, and B. A. Bernevig, Topological quantum chemistry, Nature (London) **547**, 298 (2017).

[46] M. G. Vergniory, L. Elcoro, Z. Wang, J. Cano, C. Felser, M. I. Aroyo, B. A. Bernevig, and B. Bradlyn, Graph theory data for topological quantum chemistry, Phys. Rev. E **96**, 023310 (2017).

[47] J. Cano, B. Bradlyn, Z. Wang, L. Elcoro, M. G. Vergniory, C. Felser, M. I. Aroyo, and B. A. Bernevig, Building blocks of topological quantum chemistry: Elementary band representations, Phys. Rev. B **97**, 035139 (2018).

[48] J. Zhang, W. Ji, C. Zhang, P. Li, and P. Wang, Nontrivial topology and topological phase transition in two-dimensional monolayer Tl, Phys. Chem. Chem. Phys. **20**, 24790 (2018).

[49] Y. Yao, F. Ye, X.-L. Qi, S.-C. Zhang, and Z. Fang, Spin-orbit gap of graphene: First-principles calculations, Phys. Rev. B **75**, 041401(R) (2007).

[50] Y. Li, J. Zhang, B. Zhao, Y. Xue, and Z. Yang, Constructive coupling effect of topological states and topological phase transitions in plumbene, Phys. Rev. B **99**, 195402 (2019).

[51] C. H. Hsu, Z. Q. Huang, C. P. Crisostomo, L. Yao, F. Chuang, Y. Liu, B. Wang, C. Hsu, C. Lee, H. Lin *et al.*, Two-dimensional topological crystalline insulator phase in Sb/Bi planar honeycomb with tunable Dirac gap, Sci. Rep. **6**, 18993 (2016).

[52] X.-L. Yu and J. Wu, Evolution of the topological properties of two-dimensional group IVA materials and device design, Phys. Chem. Chem. Phys. **20**, 2296 (2018).

[53] R. Yu, H. Weng, Z. Fang, X. Dai, and X. Hu, Topological node-line semimetal and Dirac semimetal state in antiperovskite Cu_3PdN, Phys. Rev. Lett. **115**, 036807 (2015).